ACS APPLIED MATERIALS & INTERFACES

Research Article

www.acsami.org

Sandwich-Structured Graphene-Fe_3O_4@Carbon Nanocomposites for High-Performance Lithium-Ion Batteries

Li Zhao,[†] Miaomiao Gao,[†] Wenbo Yue,*[,†] Yang Jiang,[†] Yuan Wang,[†] Yu Ren,[‡] and Fengqin Hu*[,†]

[†]Beijing Key Laboratory of Energy Conversion and Storage Materials, College of Chemistry, Beijing Normal University, Beijing 100875, P. R. China

[‡]National Institute of Clean-and-Low-Carbon Energy, Beijing 102209, P. R. China

Supporting Information

ABSTRACT: Advanced anode materials for high power and high energy lithium-ion batteries have attracted great interest due to the increasing demand for energy conversion and storage devices. Metal oxides (e.g., Fe_3O_4) usually possess high theoretical capacities, but poor electrochemical performances owing to their severe volume change and poor electronic conductivity during cycles. In this work, we develop a self-assembly approach for the synthesis of sandwich-structured graphene-Fe_3O_4@carbon composite, in which Fe_3O_4 nanoparticles with carbon layers are immobilized between the layers of graphene nanosheets. Compared to Fe_3O_4@carbon and bulk Fe_3O_4, graphene-Fe_3O_4@carbon composite shows superior electrochemical performance, including higher reversible capacity, better cycle and rate performances, which may be attributed to the sandwich structure of the composite, the nanosized Fe_3O_4, and the carbon layers on the surface of Fe_3O_4. Moreover, compared to the reported graphene-Fe_3O_4 composite, the particle size of Fe_3O_4 is controllable and the content of Fe_3O_4 in this composite can be arbitrarily adjusted for optimal performance. This novel synthesis strategy may be employed in other sandwich-structured nanocomposites design for high-performance lithium-ion batteries and other electrochemical devices.

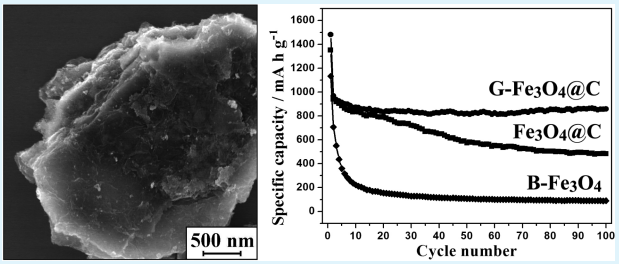

KEYWORDS: *magnetite nanoparticle, graphene, sandwich structure, lithium-ion battery*

INTRODUCTION

The development of high energy and power density lithium-ion batteries (LIBs) is very important due to the increasing demand of the energy conversion and storage devices for portable electronics and E-mobilities. As one of the promising anode materials for LIBs, metal oxides have attracted much attention owing to their high theoretical capacities, natural abundance, and low cost.[1−3] However, bulk metal oxides usually display poor cycle life and rate performance because of their huge volume change and poor electronic conductivity during the charge and discharge process.[4−6] Some effective approaches have been developed to address these issues, such as design of metal oxides with porous structure, which may effectively buffer the volume variation,[7−9] or fabrication of carbon-coated metal oxides because carbon layers could either restrain the volume change of metal oxides or enhance the electronic conductivity of the composite.[10−12] The particle size of metal oxides is another critical factor for a good electrochemical behavior. Nanosized metal oxides offer more electrochemical active sites and shorter diffusion length for Li^+ insertion than their bulk counterparts due to their large surface area and small particle size.[13−16] Moreover, the volume expansion problem can be relatively relieved by the nanosized particles, leading to the improvement of the electrochemical performances.[17,18] However, nanoparticles tend to aggregate to minimize their surface energy, seriously reducing their active reaction sites and the migration rate of Li^+ ion.[19,20] Therefore, highly dispersed metal oxide particles with small particle size and narrow particle size distribution are much desired and may theoretically display excellent electrochemical performances.

As a novel two-dimensional carbon matrix, graphene possesses many advantages, such as large specific surface area, unique mechanical property, and high electronic conductivity.[21] Thus, it is preferable to replace other carbon matrices (e.g., graphite) for supporting metal oxides because graphene nanosheets not only act as a volume buffer and electron conductor for metal oxides, but also suppress the aggregation of nanoparticles during cycles, which may highly improve the electrochemical performance of metal oxides.[22−25] In the past six years, graphene-based metal oxide composites with high capacity and cycling stability have been thoroughly explored for LIBs and supercapacitors.[26−28] However, the precise control of particle size and size distribution as well as the dispersion of particles on the surface of graphene nanosheets is still the challenges in terms of graphene-based composites. For instance, graphene-based Fe_3O_4 composites are mainly prepared through in situ growth of Fe_3O_4 nanoparticles on the surface of graphene nanosheets or coassembly of Fe_3O_4

Received: February 15, 2015
Accepted: April 17, 2015
Published: April 17, 2015

DOI: 10.1021/acsami.5b01503
ACS Appl. Mater. Interfaces 2015, 7, 9709−9715

nanoparticles and graphene nanosheets. Nevertheless, the particle size and size distribution of Fe_3O_4 cannot be controlled easily and effectively by the in situ growth method.[29−31] In addition, the content of Fe_3O_4 in the composite is limited in terms of the monodispersity of Fe_3O_4 nanoparticles on the graphene,[32,33] leading to the decrease in the theoretical capacity of the composite. However, the size and morphology of Fe_3O_4 nanoparticles are determined before self-assembly of Fe_3O_4 nanoparticles on the graphene nanosheets. Moreover, graphene nanosheets can be connected by Fe_3O_4 nanoparticles to form a sandwich structure, which may protect Fe_3O_4 nanoparticles and thereby enhance the cyclic stability. However, the number of Fe_3O_4 nanoparticles between the graphene layers rests with the quantity of the functional groups of graphene oxides (GO), and thus the loading of Fe_3O_4 is also not high enough (~55 wt %).[34] Until now, much effort has been still devoted to the exploration of high-loading metal oxides on the graphene with high capacity and cycling stability, though some graphene-based composites with low content of Fe_3O_4 were recently reported with high capacities exceeding the theoretical capacity of Fe_3O_4.[33,35]

Herein, we developed a self-assembly approach for the synthesis of sandwich-structured graphene-Fe_3O_4@carbon composite (referred as to G-Fe_3O_4@C), in which Fe_3O_4 nanoparticles with an average diameter of ~5 nm were coated by carbon layers and then immobilized between the layers of graphene nanosheets. Compared to the reported graphene-based Fe_3O_4 composite, G-Fe_3O_4@C possesses several advantages: (1) the particle size and size distribution of Fe_3O_4 are controllable; (2) high loading of Fe_3O_4 (~85 wt %) in the composite is feasible because the aggregation of Fe_3O_4 nanoparticles is prevented by carbon coating; and (3) a sandwich structure of graphene-based Fe_3O_4 composite is achieved. In addition, carbon-coated Fe_3O_4 nanoparticles without graphene (referred as to Fe_3O_4@C) and bulk Fe_3O_4 (referred as to B-Fe_3O_4) were also prepared for comparison. Compared to B-Fe_3O_4 and Fe_3O_4@C, G-Fe_3O_4@C showed superior electrochemical performance due to its unique structure. The effects of the particle size and the content of Fe_3O_4 on the performance of G-Fe_3O_4@C are also investigated.

EXPERIMENTAL SECTION

GO and Fe_3O_4@PEG nanoparticles were synthesized according to the published literature (see the Supporting Information, SI).[36,37] G-Fe_3O_4@C was synthesized by coassembly of GO-PDDA nanosheets and Fe_3O_4@PEG nanoparticles. In a typical experiment, 0.03 g of GO and 1.3 g of PDDA were dispersed in 100 mL of H_2O by ultrasonication for 0.5 h, respectively. 0.4 g of NaOH was then added into the PDDA solution with ultrasonication for another 0.5 h. Subsequently, the GO solution was added dropwise into the PDDA solution under ultrasonication. After 2 h, the GO-PDDA nanosheets was collected by centrifugation, washed with deionized water, and finally dispersed in H_2O for further use. Afterward, 40 mL of Fe_3O_4@PEG solution and 40 mL of GO-PDDA solution were diluted to 100 mL, respectively. After adjusting the pH of Fe_3O_4@PEG solution to ~8.0 with aqueous ammonia, the Fe_3O_4@PEG solution was added dropwise into the GO-PDDA solution under mild magnetic stirring. After 0.5 h, the precipitate was collected by centrifugation, washed with deionized water and dried at 60 °C. The obtained powder was then transferred into a tube furnace under N_2 protection for calcination. The temperature was increased from room temperature to 500 °C at a ramping rate of 10 °C min^{-1} and kept at that temperature for 10 min. The G-Fe_3O_4@C composite was finally obtained after being cooled down to room temperature. For comparison, the Fe_3O_4@C composite was prepared by coassembly of PDDA and Fe_3O_4@PEG nanoparticles, and calcination of the precipitate under the same conditions. The G-Fe_3O_4@C composites with different contents of Fe_3O_4 were prepared by adjusting the concentration of Fe_3O_4@PEG solution. The G-Fe_3O_4@C composites synthesized at different heating temperature or with different heating time were also explored.

Specimens were characterized by X-ray diffraction (XRD), Fourier transform infrared (FT-IR), X-ray photoelectron (XPS), Raman, thermogravimetric analysis (TGA), transmission electron microscopy (TEM), high-resolution TEM (HRTEM), and scanning electron microscope (SEM). Detailed characterization and electrochemical test methods may refer to our recent reports (see the SI).[25,27]

RESULTS AND DISCUSSION

The overall synthetic procedure of Fe_3O_4@C and G-Fe_3O_4@C is shown in Figure 1. First, Fe_3O_4 nanoparticles with an average

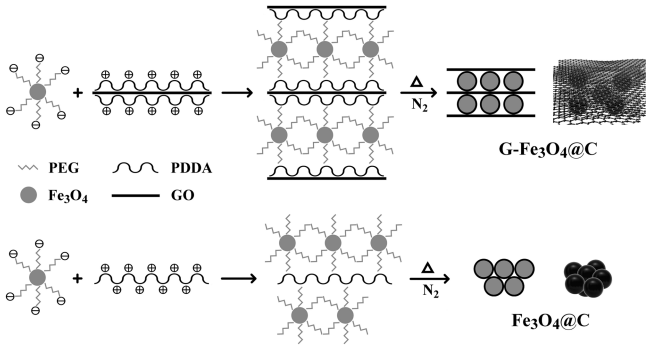

Figure 1. Schematic illustration of the synthetic route for Fe_3O_4@C and G-Fe_3O_4@C.

diameter of ~5 nm and GO were synthesized according to the published literature.[36,37] Subsequently, unlike these previous reports that the surface of Fe_3O_4 nanoparticles were positively charged by grafting of amino groups,[24,34] the surface of Fe_3O_4 nanoparticles in this work was modified by grafting of poly(ethylene glycol) bis(carboxymethyl) ether (abbreviated as HOOC—PEG—COOH) to render the oxide surface negatively charged, while the surface of GO was modified by grafting of poly(diallyldimethylammonium chloride) (abbreviated as PDDA) to render the GO surface positively charged. Accordingly, there are more electrostatic adsorption sites on the surface of GO to capture Fe_3O_4@PEG nanoparticles, giving rise to a high loading of Fe_3O_4. The strong electrostatic interaction between Fe_3O_4@PEG and GO-PDDA was also confirmed by their zeta-potentials in aqueous solution (Figure 2A). Apparently, the surfaces of Fe_3O_4@PEG and GO-PDDA are oppositely charged over a broad range of pH values. After calcination in a N_2 atmosphere, Fe_3O_4 nanoparticles were coated by carbon layers derived from PEG and PDDA, and meanwhile, GO was reduced to graphene. Besides, Fe_3O_4@C agglomerates were prepared through calcination of Fe_3O_4@PEG nanoparticles linked by PDDA.

The morphology and structure of G-Fe_3O_4@C were elucidated by SEM and TEM. Figure 2B shows the SEM image of G-Fe_3O_4@C, revealing that Fe_3O_4 nanoparticles are embedded between the transparent graphene nanosheets, and the large particles or agglomerates were hardly observed on the surface of graphene. The compact layer-by-layer stacking of the graphene nanosheets with a thickness of above 0.5 μm was also observed in the SEM image (SI Figure S1A), which is similar to that of pristine flake graphite except for the Fe_3O_4 nanoparticles

DOI: 10.1021/acsami.5b01503
ACS Appl. Mater. Interfaces 2015, 7, 9709−9715

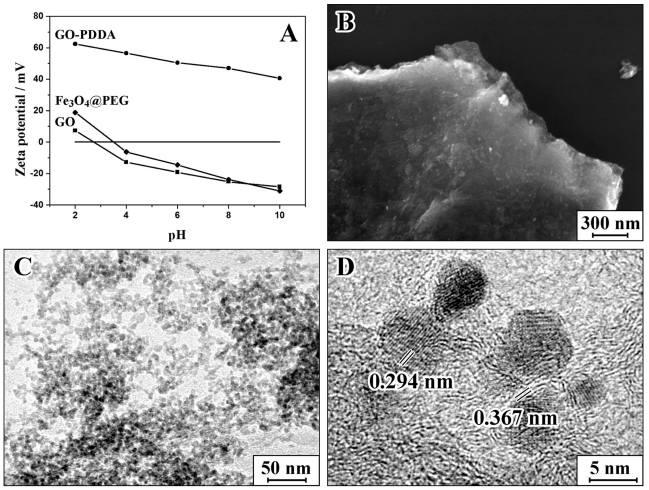

Figure 2. (A) Zeta potentials of GO, GO-PDDA, and Fe_3O_4@PEG in aqueous solution at different pH values. (B) SEM, (C) TEM, and (D) HRTEM images of G-Fe_3O_4@C.

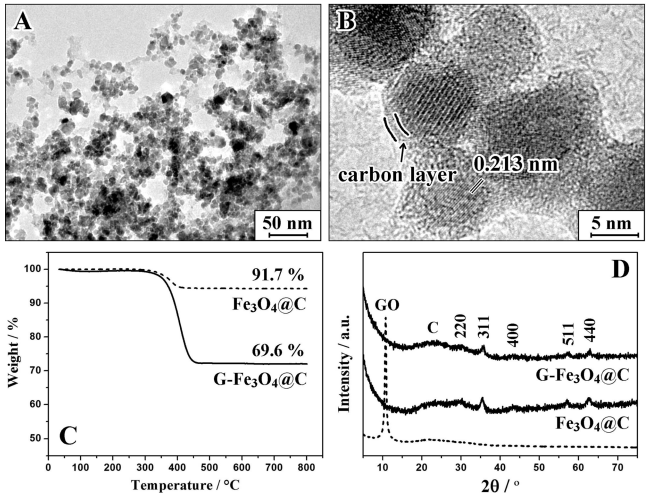

Figure 3. (A) TEM and (B) HRTEM images of Fe_3O_4@C. (C) TGA curves of G-Fe_3O_4@C and Fe_3O_4@C. (D) XRD patterns of GO, G-Fe_3O_4@C, and Fe_3O_4@C.

inside the interlayer space. To further explore the inner morphology, TEM image of G-Fe_3O_4@C is shown in Figure 2C. It is worth noting that the Fe_3O_4 nanoparticles with an average diameter of ∼5 nm are strongly attached to the graphene nanosheets even after ultrasonic treatment, implying the strong interaction between the Fe_3O_4 nanoparticles and graphene nanosheets through carbon layers. Moreover, the Fe_3O_4 nanoparticles are homogeneously dispersed on the surface of graphene nanosheets without any obvious aggregation. The HRTEM image (Figure 2D) reveals that each nanoparticle on the graphene surface is a single crystal, and the distance of crystal lattice fringes is ∼0.294 nm, corresponding to the (220) plane of Fe_3O_4 crystal.[38] In addition, few-layer graphene nanosheets with a lattice spacing of ∼0.367 nm were observed around the crystals, implying that the Fe_3O_4 nanoparticles are embedded between graphene nanosheets. G-Fe_3O_4@C was further characterized by the XPS, FT−IR, and Raman spectroscopy to evaluate the reduction degree of the GO component (SI Figure S2), which may be important to the electrochemical property of G-Fe_3O_4@C. The results indicate that GO was highly reduced under thermal treatment.[39,40]

The Fe_3O_4@PEG precursor was also observed by TEM to ensure the size distribution of the synthesized Fe_3O_4 nanoparticles. The TEM image of Fe_3O_4@PEG (SI Figure S3A) illustrates that Fe_3O_4@PEG nanoparticles were highly dispersed in the suspension because of the electrostatic repulsion among the nanoparticles (Figure 2A). The histogram of the nanoparticle size based on statistical results (SI Figure S3B) indicates that the average size of Fe_3O_4@PEG nanoparticles is 5.1 nm, similar to the particle size of Fe_3O_4 in G-Fe_3O_4@C. After connected by PDDA and carbonization, Fe_3O_4 nanoparticles aggregated seriously though various pores were formed by the aggregation (SI Figure S1B), and some large particles (8−10 nm) were also observed (Figure 3A), which may be attributed to the growth of Fe_3O_4 under high temperature. However, according to the HRTEM image (Figure 3B), a carbon layer of less than 1 nm formed on the surface of Fe_3O_4 nanoparticles, which should protect the nanoparticles and restrain their severe growth. The TGA curves of Fe_3O_4@C (Figure 3C) also confirmed the presence of carbon layers by virtue of the content of Fe_3O_4 in Fe_3O_4@C (∼91.7 wt %, calculated from the weight of the calcined product Fe_2O_3). A possible explanation is that the carbon layer is not distributed across the surface of the nanoparticles considering the distribution of carbon source (i.e., PDDA) in the agglomerates, leading to the growth of some exposed nanoparticles. On the contrary, the agglomerates and large particles are negligible on the graphene surface in spite of high content of Fe_3O_4 in G-Fe_3O_4@C (∼69.6 wt %), implying that graphene nanosheets can prevent the particle aggregation and growth since Fe_3O_4 nanoparticles are dispersed and immobilized on the surface of graphene. The characteristic peaks in the XRD patterns of G-Fe_3O_4@C and Fe_3O_4@C (Figure 3D) are both indexed into the cubic Fe_3O_4 structure (space group *Fd*-3*m*, a = 0.8391 nm),[41] in accordance with the HRTEM results. Besides, a broad peak at around 23° appears in both XRD patterns, suggesting the presence of amorphous carbon (derived from PDDA and PEG) in the composites, while the feature diffraction peak for GO (∼11°) disappears in the XRD pattern of G-Fe_3O_4@C, deducing that GO is reduced to graphene.

The unique structure of G-Fe_3O_4@C may be beneficial to improving its electrochemical performance, and thus the electrochemical properties of B-Fe_3O_4, Fe_3O_4@C, and G-Fe_3O_4@C were investigated by cyclic voltammetry and galvanostatic measurements. Figure 4A shows the first-cycle charge and discharge curves for these samples with an obvious flat plateau, indicative of the conversion of Fe_3O_4 to Fe. The large initial capacity (∼1481 mA h g^{-1} for G-Fe_3O_4@C, ∼1350 mA h g^{-1} for Fe_3O_4@C and ∼1133 mA h g^{-1} for B-Fe_3O_4) and capacity loss can be attributed to the formation of a solid electrolyte interface (SEI) layer on the surface of Fe_3O_4-based electrode. These reactions are also supported by the cyclic voltammograms (CV) of G-Fe_3O_4@C. SI Figure S4A shows the CV curves in the first, second, third, and sixth scanning cycles. In the first cathodic scan, two reduction peaks were observed at ∼0.69 and ∼0.91 V, corresponding to the reduction of Fe_3O_4 to Fe and the formation of SEI layer on the surface of Fe_3O_4. In the first anodic scan, a broad peak was recorded at about ∼1.8 V, indicating the corresponding reversible reaction. In the subsequent cycles, only one reduction peak was left and slightly shifted to ∼0.76 V. The CV curves after the first cycle

DOI: 10.1021/acsami.5b01503
ACS Appl. Mater. Interfaces 2015, 7, 9709−9715

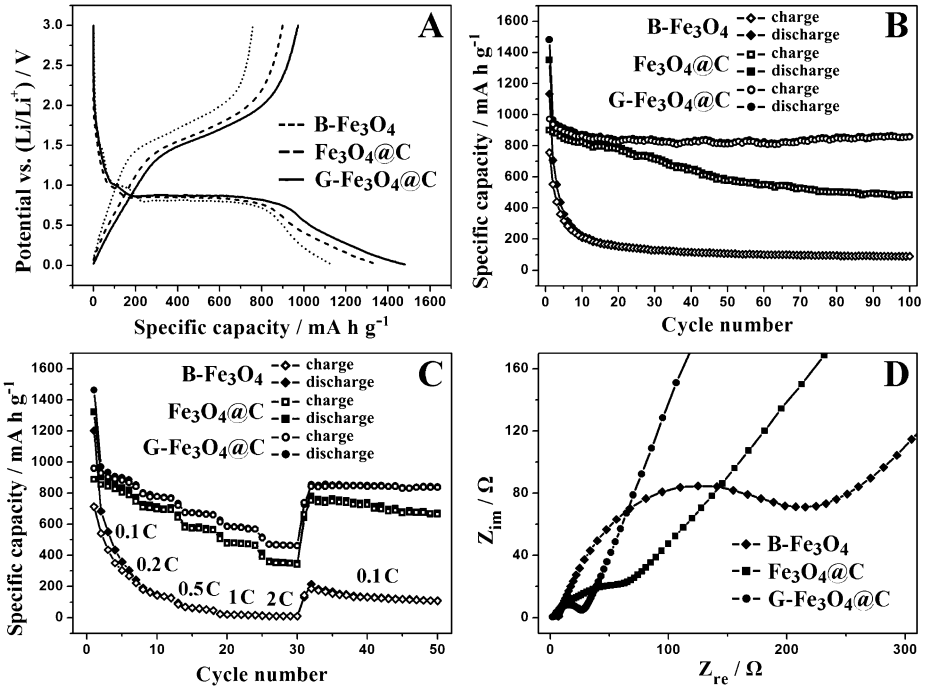

Figure 4. (A) The first cycle charge−discharge curves of B-Fe_3O_4, Fe_3O_4@C, and G-Fe_3O_4@C at 0.1 C. (B) Cycle and (C) rate performances of these samples at 0.1 C and 0.1−2 C. (D) Electrochemical impedance spectra of these samples after 3 cycles.

almost overlapped, reflecting a good reversibility. The cycle and rate performances of these samples are shown in Figure 4B,C. At a current density of 0.1 C, the capacity of B-Fe_3O_4 decreases rapidly in the initial several cycles and only ∼90 mA h g^{-1} is achieved after 100 cycles, whereas G-Fe_3O_4@C exhibits a higher reversible capacity of ∼860 mA h g^{-1} after 100 cycles, still better than those of some reported graphene-based Fe_3O_4 composites (500−700 mA h g^{-1}) prepared by either in situ growth method or self-assembly method.[31,32,34] The cycling stability of G-Fe_3O_4@C is also impressive in view of a capacity retention of 90% versus the second cycle (∼960 mA h g^{-1}). Fe_3O_4@C displays good cycle performance in the initial 20 cycles, but the capacity fades during the following cycles and finally maintains at ∼480 mA h g^{-1}. When the current density increases to 2 C, the capacity of G-Fe_3O_4@C remains at ∼460 mA h g^{-1}, still higher than that of B-Fe_3O_4 (∼10 mA h g^{-1}) and Fe_3O_4@C (∼350 mA h g^{-1}). Moreover, a capacity of ∼840 mA h g^{-1} is recoverable for G-Fe_3O_4@C when the current rate returns to 0.1 C, validating its good cycling stability. To further study the superior performance of G-Fe_3O_4@C, EIS measurements of these samples were performed after 3 cycles. SI Figure S4B shows the equivalent circuit model for EIS measurements. Apparently, the diameter of the semicircle for G-Fe_3O_4@C in the Nyquist plot is much smaller than those for B-Fe_3O_4 and Fe_3O_4@C (Figure 4D), suggesting that the graphene substrate facilitates the electron transport (see SI Table S1), and thereby improves the rate capability of G-Fe_3O_4@C.

The excellent electrochemical property of G-Fe_3O_4@C may be attributed to its unique sandwich structure: (1) ultrasmall Fe_3O_4 nanoparticles are homogeneously dispersed on the surface of graphene, providing a large electrode/electrolyte interface and reducing the diffusion paths of Li^+ ions; (2) the carbon layer on the surface of Fe_3O_4 nanoparticles prevents the particle aggregation even though high loading of Fe_3O_4 is pursued and restrains the volume change of Fe_3O_4 during cycles; (3) the Fe_3O_4 nanoparticles are further protected by graphene nanosheets, which act as a strain buffer to accommodate the volume change; and (4) the carbon layer and graphene nanosheets highly improve the electronic conductivity of the composite electrode.

The particle size and the content of Fe_3O_4 may highly influence the performance of G-Fe_3O_4@C, and hence the experimental comparison on various Fe_3O_4 contents and particle sizes was carried out. The dose-ratio of Fe_3O_4@PEG and graphene was adjusted to obtain various content of Fe_3O_4 in G-Fe_3O_4@C, denoted as G-Fe_3O_4@C-55 and G-Fe_3O_4@C-85 according to the weight percent of Fe_3O_4 calculated from the TGA curves (Figure 5A,C). TEM images (Figure 5B,D) show that the Fe_3O_4 nanoparticles were highly separated on the surface of graphene when the content of Fe_3O_4 is reduced (∼54.3 wt %), while the graphene nanosheets are covered by a

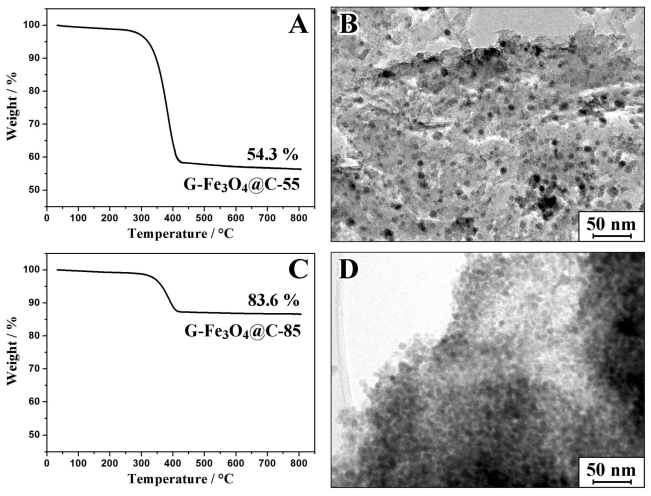

Figure 5. TGA curves and TEM images of (A, B) G-Fe_3O_4@C-55 and (C, D) G-Fe_3O_4@C-85.

DOI: 10.1021/acsami.5b01503
ACS Appl. Mater. Interfaces 2015, 7, 9709−9715

homogeneous layer of Fe_3O_4 nanoparticles when the content of Fe_3O_4 is enhanced (~83.6 wt %). However, the effect of heating temperature and time on the particle size of Fe_3O_4 was also explored (G-Fe_3O_4@C-500−30 was synthesized at 500 °C for 30 min and G-Fe_3O_4@C-700−10 was synthesized at 700 °C for 10 min). According to the TEM images (Figure 6A,C), the particle size of Fe_3O_4 increased with the increase of either heating temperature or heating time, and the former factor has greater influence on the particle size. The distinct interfaces among the particles were observed in the HRTEM image (Figure 6B), implying that the large particle consists of several small nanoparticles. After calcination at higher temperature, the adjacent nanoparticles tend to fuse together and the interfaces among the particles were hardly distinguished (Figure 6D), leading to form larger polycrystalline particles.

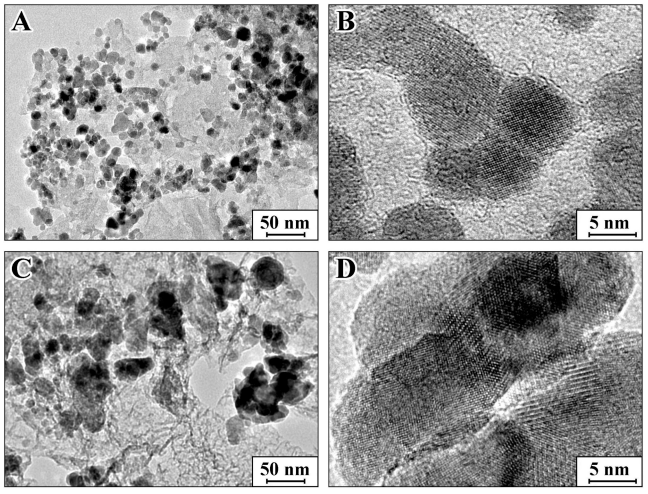

Figure 6. TEM and HRTEM images of (A, B) G-Fe_3O_4@C-500−30 and (C, D) G-Fe_3O_4@C-700−10.

The cycle performances of the above samples as well as G-Fe_3O_4@C (~70 wt % Fe_3O_4, synthesized at 500 °C for 10 min) are shown in Figure7, and the reversible capacity of each sample after 100 cycles is listed in SI Table S2. Compared to G-Fe_3O_4@C, G-Fe_3O_4@C-55 shows stable cycle performance as well, but its reversible capacities are relatively lower owing to low content of Fe_3O_4 in the composite. Moreover, the decrease of Fe_3O_4 content may also reduce the volumetric capacity of the composite due to its relatively low density,[18] and thus high content of metal oxides in carbon−metal oxide composites is desired on the premise of stable cycling. However, the capacity of G-Fe_3O_4@C-85 decreases gradually with increasing cycle number though its reversible capacities are much high in the initial several cycles, possibly because the space between nanoparticles for accommodating the volume change of Fe_3O_4 was minimized by excessive loading of Fe_3O_4 on the graphene surface. G-Fe_3O_4@C-500−30 and G-Fe_3O_4@C-700−10 exhibit worse cycle performances due to the formation of large particles, which aggravates the pulverization problem caused by the volume change of Fe_3O_4 even though it is partially restrained by graphene nanosheets. Therefore, the synthetic conditions should be rigidly controlled in order to limit the particle size of Fe_3O_4 and pursue exceptional lithium anodic performance.

CONCLUSIONS

We developed a novel strategy for the preparation of sandwich-structured graphene-Fe_3O_4 composites with several characteristics including high content of Fe_3O_4, ultrasmall Fe_3O_4 nanoparticles and carbon layers on the surface of Fe_3O_4. Compared to bulk Fe_3O_4 and carbon-coated Fe_3O_4, the sandwich-structured composite exhibits higher reversible capacity and better cycle/rate performance due to the unique

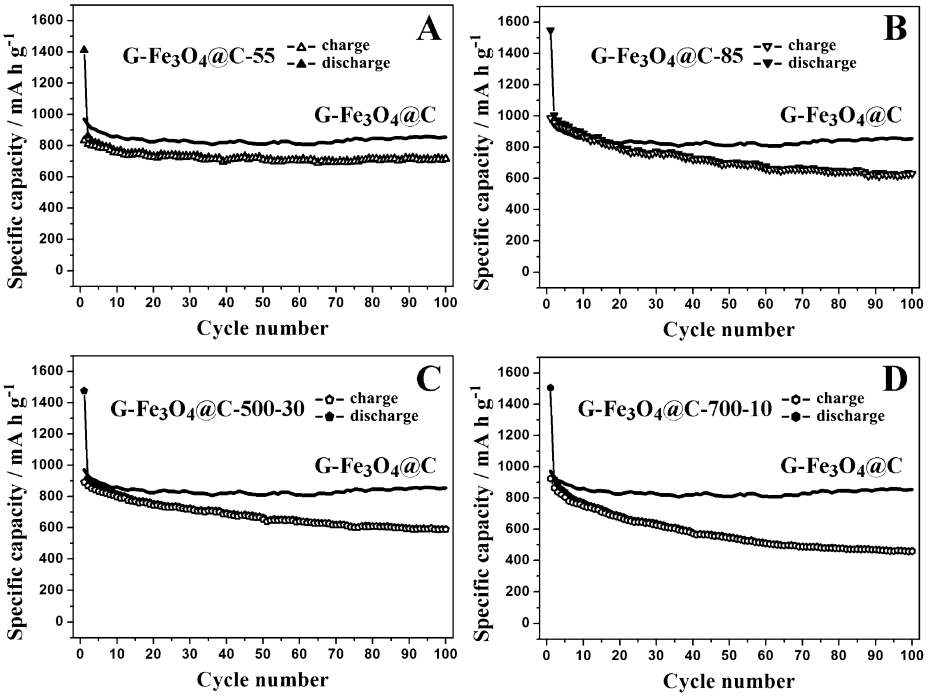

Figure 7. Cycle performances of (A) G-Fe_3O_4@C-55, (B) G-Fe_3O_4@C-85, (C) G-Fe_3O_4@C-500−30, and (D) G-Fe_3O_4@C-700−10 at 0.1 C. G-Fe_3O_4@C contained ~70 wt % Fe_3O_4 nanoparticles and were synthesized at 500 °C for 10 min.

DOI: 10.1021/acsami.5b01503
ACS Appl. Mater. Interfaces 2015, 7, 9709−9715

structure. The graphene substrate and the carbon layer on the surface of Fe_3O_4 may avoid the aggregation of nanoparticles, buffer the volume change of Fe_3O_4 and restrain the growth of nanoparticles to a certain extent, which are important to the superior electrochemical performance of the composite. This study offers an alternative strategy for the preparation of other sandwich-structured nanocomposites as high-performance electrodes for lithium-ion batteries or other electrochemical devices.

■ ASSOCIATED CONTENT

Supporting Information

SEM images of G-Fe_3O_4@C and Fe_3O_4@C. XPS, FT−IR, and Raman spectra of G-Fe_3O_4@C. TEM image and size distribution histogram of Fe_3O_4@PEG. CV curves of G-Fe_3O_4@C. Randles equivalent circuit for samples. The Supporting Information is available free of charge on the ACS Publications website at DOI: 10.1021/acsami.5b01503.

■ AUTHOR INFORMATION

Corresponding Authors

*Tel: 86-10-58894229. Fax: 86-10-58892075. E-mail: wbyue@bnu.edu.cn(W.Y.).

*E-mail: fqhu@bnu.edu.cn (F.H.).

Notes

The authors declare no competing financial interest.

■ ACKNOWLEDGMENTS

This work is financially supported by the Fundamental Research Funds for the Central Universities, National Natural Science Foundation of China (21101014, 21103012, and 21273022), and Beijing Municipal Natural Science Foundation (2142017).

■ REFERENCES

(1) Aricò, A. S.; Bruce, P.; Scrosati, B.; Tarascon, J.-M.; van Schalkwijk, W. Nanostructured Materials for Advanced Energy Conversion and Storage Devices. *Nat. Mater.* **2005**, *4*, 366−377.

(2) Armand, M.; Tarascon, J.-M. Researchers Must Find a Sustainable Way of Providing the Power Our Modern Lifestyles Demand. *Nature* **2008**, *451*, 652−657.

(3) Ming, J.; Park, J.-B.; Sun, Y.-K. Encapsulation of Metal Oxide Nanocrystals into Porous Carbon with Ultrahigh Performances in Lithium-Ion Battery. *ACS Appl. Mater. Interfaces* **2013**, *5*, 2133−2136.

(4) Reddy, M. V.; Subba Rao, G. V.; Chowdari, B. V. R. Metal Oxides and Oxysalts as Anode Materials for Li Ion Batteries. *Chem. Rev.* **2013**, *113*, 5364−5457.

(5) Gwon, H.; Hong, J.; Kim, H.; Seo, D.-H.; Jeon, S.; Kang, K. Recent Progress on Flexible Lithium Rechargeable Batteries. *Energy Environ. Sci.* **2014**, *7*, 538−551.

(6) Yue, W. B.; Jiang, S. H.; Huang, W. J.; Gao, Z. Q.; Li, J.; Ren, Y.; Zhao, X. H.; Yang, X. J. Sandwich-Structural Graphene-Based Metal Oxides as Anode Materials for Lithium-Ion Batteries. *J. Mater. Chem. A* **2013**, *1*, 6928−6933.

(7) Ren, Y.; Ma, Z.; Bruce, P. G. Ordered Mesoporous Metal Oxides: Synthesis and Applications. *Chem. Soc. Rev.* **2012**, *41*, 4909−4927.

(8) Vu, A.; Qian, Y. Q.; Stein, A. Porous Electrode Materials for Lithium-Ion Batteries—How to Prepare Them and What Makes Them Special. *Adv. Energy Mater.* **2012**, *2*, 1056−1085.

(9) Yang, S.; Yue, W. B.; Zhu, J.; Ren, Y.; Yang, X. J. Graphene-Based Mesoporous SnO_2 with Enhanced Electrochemical Performance for Lithium-Ion Batteries. *Adv. Funct. Mater.* **2013**, *23*, 3570−3576.

(10) Su, Y. Z.; Li, S.; Wu, D. Q.; Zhang, F.; Liang, H. W.; Gao, P. F.; Cheng, C.; Feng, X. L. Two-Dimensional Carbon-Coated Graphene/Metal Oxide Hybrids for Enhanced Lithium Storage. *ACS Nano* **2012**, *6*, 8349−8356.

(11) Yang, S. J.; Nam, S.; Kim, T.; Im, J. H.; Jung, H.; Kang, J. H.; Wi, S.; Park, B.; Park, C. R. Preparation and Exceptional Lithium Anodic Performance of Porous Carbon-Coated ZnO Quantum Dots Derived from a Metal−Organic Framework. *J. Am. Chem. Soc.* **2013**, *135*, 7394−7397.

(12) Yue, W. B.; Tao, S. S.; Fu, J. M.; Gao, Z. Q.; Ren, Y. Carbon-Coated Graphene−Cr_2O_3 Composites with Enhanced Electrochemical Performances for Li-Ion Batteries. *Carbon* **2013**, *65*, 97−104.

(13) Bruce, P. G.; Scrosati, B.; Tarascon, J.-M. Nanomaterials for Rechargeable Lithium Batteries. *Angew. Chem., Int. Ed.* **2008**, *47*, 2930−2946.

(14) Lee, K. T.; Cho, J. Roles of Nanosize in Lithium Reactive Nanomaterials for Lithium Ion Batteries. *Nano Today* **2011**, *6*, 28−41.

(15) Wang, S. B.; Xing, Y. L.; Xu, H. Z.; Zhang, S. C. MnO Nanoparticles Interdispersed in 3D Porous Carbon Framework for High Performance Lithium-Ion Batteries. *ACS Appl. Mater. Interfaces* **2014**, *6*, 12713−12718.

(16) Zhang, K.; Zhao, W.; Lee, J.-T.; Jang, G.; Shi, X. J.; Park, J. H. A Magnetic Field Assisted Self-Assembly Strategy towards Strongly Coupled Fe_3O_4 Nanocrystal/rGO Paper for High-Performance Lithium Ion Batteries. *J. Mater. Chem. A* **2014**, *2*, 9636−9644.

(17) Poizot, P.; Laruelle, S.; Grugeon, S.; Dupont, L.; Tarascon, J.-M. Nano-Sized Transition-Metal Oxides as Negative-Electrode Materials for Lithium-Ion Batteries. *Nature* **2000**, *407*, 496−499.

(18) Ren, Y.; Liu, Z.; Pourpoint, F.; Armstrong, A. R.; Grey, C. P.; Bruce, P. G. Nanoparticulate TiO_2(B): An Anode for Lithium-Ion Batteries. *Angew. Chem., Int. Ed.* **2012**, *51*, 2164−2167.

(19) Yu, S.-H.; Conte, D. E.; Baek, S.; Lee, D.-C.; Park, S.-K.; Lee, K. J.; Piao, Y. Z.; Sung, Y.-E.; Pinna, N. Structure-Properties Relationship in Iron Oxide-Reduced Graphene Oxide Nanostructures for Li-Ion Batteries. *Adv. Funct. Mater.* **2013**, *23*, 4293−4305.

(20) Chen, Y.; Song, B. H.; Lu, L.; Xue, J. M. Ultra-Small Fe_3O_4 Nanoparticle Decorated Graphene Nanosheets with Superior Cyclic Performance and Rate Capability. *Nanoscale* **2013**, *5*, 6797−6803.

(21) Novoselov, K. S.; Geim, A. K.; Morozov, S. V.; Jiang, D.; Katsnelson, M. I.; Grigorieva, I. V.; Dubonos, S. V.; Firsov, A. A. Two-Dimensional Gas of Massless Dirac Fermions in Graphene. *Nature* **2005**, *438*, 197−200.

(22) Wang, H. L.; Cui, L. F.; Yang, Y.; Casalongue, H. S.; Robinson, J. T.; Liang, Y. Y.; Cui, Y.; Dai, H. J. Mn_3O_4−Graphene Hybrid as a High-Capacity Anode Material for Lithium Ion Batteries. *J. Am. Chem. Soc.* **2010**, *132*, 13978−13980.

(23) Chen, Y.; Yan, C. L.; Schmidt, O. G. Strain-Driven Formation of Multilayer Graphene/GeO_2 Tubular Nanostructures as High-Capacity and Very Long-Life Anodes for Lithium-Ion Batteries. *Adv. Energy Mater.* **2013**, *3*, 1269−1274.

(24) Wei, W.; Yang, S. B.; Zhou, H. X.; Lieberwirth, I.; Feng, X. L.; Müllen, K. 3D Graphene Foams Cross-Linked with Pre-Encapsulated Fe_3O_4 Nanospheres for Enhanced Lithium Storage. *Adv. Mater.* **2013**, *25*, 2909−2914.

(25) Guo, R.; Yue, W. B.; An, Y. M.; Ren, Y.; Yan, X. Graphene-Encapsulated Porous Carbon-ZnO Composites as High-Performance Anode Materials for Li-Ion Batteries. *Electrochim. Acta* **2014**, *135*, 161−167.

(26) Xia, G. F.; Li, N.; Li, D. Y.; Liu, R. Q.; Wang, C.; Li, Q.; Lü, X. J.; Spendelow, J. S.; Zhang, J. L.; Wu, G. Graphene/Fe_2O_3/SnO_2 Ternary Nanocomposites as a High-Performance Anode for Lithium Ion Batteries. *ACS Appl. Mater. Interfaces* **2013**, *5*, 8607−8614.

(27) Tao, S. S.; Yue, W. B.; Zhong, M. Y.; Chen, Z. J.; Ren, Y. Fabrication of Graphene-Encapsulated Porous Carbon−Metal Oxide Composites as Anode Materials for Lithium-Ion Batteries. *ACS Appl. Mater. Interfaces* **2014**, *6*, 6332−6339.

(28) Liu, M. M.; Sun, J. In Situ Growth of Monodisperse Fe_3O_4 Nanoparticles on Graphene as Flexible Paper for Supercapacitor. *J. Mater. Chem. A* **2014**, *2*, 12068−12074.

(29) Zhang, M.; Lei, D. N.; Yin, X. M.; Chen, L. B.; Li, Q. H.; Wang, Y. G.; Wang, T. H. Magnetite/Graphene Composites: Microwave

DOI: 10.1021/acsami.5b01503
ACS Appl. Mater. Interfaces 2015, 7, 9709−9715

Irradiation Synthesis and Enhanced Cycling and Rate Performances for Lithium Ion Batteries. *J. Mater. Chem.* **2010**, *20*, 5538−5543.
(30) Zhang, M.; Jia, M. Q.; Jin, Y. H. Fe_3O_4/Reduced Graphene Oxide Nanocomposite as High Performance Anode for Lithium Ion Batteries. *Appl. Surf. Sci.* **2012**, *261*, 298−305.
(31) Vargas, C.; Caballero, Á.; Morales, J. Enhanced Electrochemical Performance of Maghemite/Graphene Nanosheets Composite as Electrode in Half and Full Li−Ion Cells. *Electrochim. Acta* **2014**, *130*, 551−558.
(32) Hsieh, C.-T.; Lin, J.-Y.; Mo, C.-Y. Improved Storage Capacity and Rate Capability of Fe_3O_4−Graphene Anodes for Lithium-Ion Batteries. *Electrochim. Acta* **2011**, *58*, 119−124.
(33) Chen, W. F.; Li, S. R.; Chen, C. H.; Yan, L. F. Self-Assembly and Embedding of Nanoparticles by In Situ Reduced Graphene for Preparation of a 3D Graphene/Nanoparticle Aerogel. *Adv. Mater.* **2011**, *23*, 5679−5683.
(34) Yoon, T.; Kim, J.; Kim, J.; Lee, J. K. Electrostatic Self-Assembly of Fe_3O_4 Nanoparticles on Graphene Oxides for High Capacity Lithium-Ion Battery Anodes. *Energies* **2013**, *6*, 4830−4840.
(35) Liang, C. L.; Zhai, T.; Wang, W.; Chen, J.; Zhao, W. X.; Lu, X. H.; Tong, Y. X. Fe_3O_4/Reduced Graphene Oxide with Enhanced Electrochemical Performance towards Lithium Storage. *J. Mater. Chem. A* **2014**, *2*, 7214−7220.
(36) Hu, F. Q.; Jia, Q. J.; Li, Y. L.; Gao, M. Y. Facile Synthesis of Ultrasmall PEGylated Iron Oxide Nanoparticles for Dual-Contrast T1- and T2-weighted Magnetic Resonance Imaging. *Nanotechnology* **2011**, *22*, 245604.
(37) Hummers, W. S.; Offeman, R. E. Preparation of Graphitic Oxide. *J. Am. Chem. Soc.* **1958**, *80*, 1339−1339.
(38) Zhang, D. H.; Zhou, C.; Sun, Z. H.; Wu, L. Z.; Tung, C. H.; Zhang, T. R. Magnetically Recyclable Nanocatalysts (MRNCs): A Versatile Integration of High Catalytic Activity and Facile Recovery. *Nanoscale* **2012**, *4*, 6244−6255.
(39) Shang, L.; Bian, T.; Zhang, B. H.; Zhang, D. H.; Wu, L. Z.; Tung, C. H.; Yin, Y. D.; Zhang, T. R. Graphene-Supported Ultrafine Metal Nanoparticles Encapsulated by Mesoporous Silica: Robust Catalysts for Oxidation and Reduction Reactions. *Angew. Chem., Int. Ed.* **2014**, *53*, 250−254.
(40) Guo, R.; Zhao, L.; Yue, W. B. Assembly of Core−Shell Structured Porous Carbon−Graphene Composites as Anode Materials for Lithium-Ion Batteries. *Electrochim. Acta* **2015**, *152*, 338−344.
(41) Zhang, D. H.; Shang, L.; Shen, J.; Shi, Z.; Wu, L. Z.; Tung, C. H.; Zhang, T. R. A Mild One-Step Solvothermal Route to Truncated Octahedral Magnetite Crystals. *Particuology* **2014**, *15*, 51−55.

DOI: 10.1021/acsami.5b01503
ACS Appl. Mater. Interfaces 2015, 7, 9709−9715